Journal of the European Ceramic Society 44 (2024) 7791–7800

Contents lists available at ScienceDirect

Journal of the European Ceramic Society

journal homepage: www.elsevier.com/locate/jeurceramsoc

Tuning the rheological properties of paraffin-wax ceramic feedstocks for deposition with thermoplastic 3D printing

Ipeknaz Özden Moser [a,b,*], Milan Vukšić [a], Matevž Dular [c], Aljaž Iveković [a,**], Andraž Kocjan [a]

[a] Department for Nanostructured Materials, Jožef Stefan Institute, Jamova 39, Ljubljana 1000, Slovenia
[b] Jožef Stefan International Postgraduate School, Jamova 39, Ljubljana 1000, Slovenia
[c] Faculty of Mechanical Engineering, University of Ljubljana, Askerceva 6, Ljubljana 1000, Slovenia

ARTICLE INFO

Keywords:
Additive manufacturing
Material jetting
Colloidal processing
Zirconia
Rheology

ABSTRACT

Droplet deposition with material-jetting methods such as thermoplastic 3D printing (T3DP) depends greatly on the rheological properties of the feedstocks. This study investigated the effect of particle interactions and the degree of weak flocculation on the shear thinning behaviour, the yield stress and the storage/loss moduli of paraffin-wax-based feedstocks containing 40 vol% of zirconia (3Y-TZP) micron-sized powder. Steric stabilization of the feedstocks was provided by varying the ratios of the surfactants with different chain lengths, i.e., stearic acid (2.4 nm) and Solsperse 3000® (10 nm), which in turn affected the dynamics of the droplet formation and the quality of the layers when jetting non-Newtonian, thermoplastic ceramic feedstocks. The results of the study extend the guidelines for the processing of printable feedstocks used in T3DP additive manufacturing.

1. Introduction

Thermoplastic 3D printing (T3DP), also referred to as multi-material jetting [1], is a drop-on-demand material-jetting technology where a wax-based thermoplastic suspension (referred to as the feedstock) [2] consisting of sterically stabilized ceramic particles is deposited in the form of micron-sized droplets with a controlled frequency and a resolution superior to fused-deposition modelling, but inferior to lithography-based additive manufacturing [3,4]. During the deposition the droplets fuse and solidify to form lines that further fuse to form the layers of a ceramic green body, where the infill strategy can affect the final properties of the parts [5]. A high solids loading (>40 vol%) of the feedstock is required to ensure high green densities with minimal shrinkage and porosity after the thermal debinding and sintering processes [6–8].

During T3DP, droplets of feedstock are extruded under the high shear rates present at the nozzle (10^5 s^{-1}) in a piezo-activated printhead [9] [10]. According to Weingarten et al. [11] the feedstock should exhibit a shear thinning behaviour with viscosities below 100, 20 and 1 Pa·s for shear rates below 10, 100, and 5000 s^{-1}, respectively. The improper feedstock composition and its rheological behaviour (and/or printing settings) would result in flaws such as continuous flow, sputtering or collecting on the nozzle [12].

The flow behaviour of ceramic suspensions is governed by the colloidal interparticle interactions determined by the solids loading, the amount of surfactant and the length of its chain. Similar to T3DP, for low-pressure injection molding (LPIM), wax-based ceramic feedstocks with a low viscosity are used [13]. These LPIM feedstocks are known to have weakly flocculated particles and a consequential yield point behaviour [14] required for shape stability during debinding [15]. It was shown for paraffin-wax-based feedstocks with a high solids loading of A16 alumina, used for LPIM applications, that they had yield stress values of 100–200 Pa at 70 °C [14]. The dependence of the yield stress on the chain length of the surfactant for feedstocks with 47 vol% of solids loading of A16 powder, used for LPIM applications, was also shown where surfactants with C12 resulted in a yield stress of 500 Pa, and feedstocks with C18 had a yield stress below 100 Pa [16].

Stearic acid is commonly used as a surfactant for the dispersion of oxide particles [7], due to its ability to attach to the surface of the particle with a polar group (COOH-) while a non-polar hydrocarbon tail spreads into the binder [17], forming a steric barrier [14,16,18]. However, such a barrier is insufficient to ensure complete steric stabilization due to its short chain length, and at zero-to-low shear rates the particles are weakly flocculated at the secondary minimum [19]. The strength of

* Corresponding author at: Department for Nanostructured Materials, Jožef Stefan Institute, Jamova 39, Ljubljana 1000, Slovenia.
** Corresponding author.
E-mail addresses: ipeknaz.ozden@ijs.si (I. Özden Moser), aljaz.ivekovic@ijs.si (A. Iveković).

https://doi.org/10.1016/j.jeurceramsoc.2024.05.057
Received 12 December 2023; Received in revised form 15 May 2024; Accepted 20 May 2024
Available online 23 May 2024

Table 1
Compositions of feedstocks with different surfactant ratios.

Feedstock	Powder loading vol%	SA mg/m^2	S3 mg/m^2	SA/S3 ratio
100 SA	40	1.25	0	100/0
15 S3		1.06	0.3	85/15
25 S3		0.93	0.5	75/25
50 S3		0.625	1	50/50
75 S3		0.31	1.5	25/75
100 S3		0	2	0/100

the particle network and consequently the value of the yield point [34] are dependent on many factors such as the length and amount of the surfactant, the solids loading, the particle size and the temperature [13,14,16].

While existing knowledge about the preparation and properties of feedstocks for LPIM applications can serve as a guideline for the feedstocks used in T3DP, the exact feedstock composition and the degree of weak flocculation can vary due to different process specifics. Namely, during LPIM, the molten feedstock is directly filled into the mould with the help of an applied pressure. In T3DP, however, the feedstock undergoes several stages of droplet jetting, i.e., extrusion, deposition and solidification, where it is subjected to large variations in shear rates and, thus, in the rheological behaviour. Additionally, a decrease in the feedstock temperature occurs, after being extruded from the hot nozzle, while airborne and deposited on the cooler print bed, where the droplet finally solidifies.

The present study aimed to investigate the relationships between the degree of weak flocculation and the rheological behaviour on the printability of feedstocks used for T3DP applications. For this purpose, paraffin-wax feedstocks containing zirconia powder dispersed with different ratios of stearic acid and Solsperse 3000® (exhibiting a 4-times-longer chain length) were prepared. The rheological properties of the feedstocks (shear thinning behaviour, yield stress, storage and loss moduli) were investigated to establish their effect on the droplet formation and the outcome of the printing. Single layers were printed and characterized for surface roughness, which served as an indicator of the resolution that could be achieved with each feedstock. In this context our research was able to provide insights into the characteristics and printing behaviour of non-Newtonian fluids such as paraffin-wax-based zirconia feedstock used for material jetting.

2. Materials and methods

2.1. Materials

Yttria-stabilized zirconia powder (TZ-3YS-E, TOSOH, Japan) was employed in this study. According to the manufacturer's specifications it has a specific surface area and a crystallite size of 7 m^2/g and 90 nm, respectively. The particle size distribution was determined with a laser scattering device (HORIBA LA-920 HORIBA) and by dispersing a small amount of powder into the measuring cell containing distilled water and Dolapix CE64 as a surfactant. Prior to measurement, a 3-minute ultrasonic treatment with 60 % amplitude was applied to break the agglomerates. This was followed by a 5-minute ultrasonic treatment during the measurement.

Paraffin wax (Sigma-Aldrich, LOT no: MKCN8112) with a melting point of ≥65 °C was used as a thermoplastic solvent. Stearic acid (SA), ($C_{17}H_{35}$-COOH), (Sigma-Aldrich, Missouri, United States), with a chain length of 2.4 nm [20], and hyperdispersant Solsperse 3000® (S3), ($C_{90}H_{172}O_{10}$), (Lubrizol, Ohio, United States), with a chain length of 10 nm [21], were used as the surfactants.

2.2. Feedstocks

The feedstocks were prepared by manually mixing the required amounts of surfactants in the molten paraffin wax at 100 °C. Once the surfactant was dissolved in the wax, zirconia powder, which was dried for 2 hours in an oven at 120 °C, was gradually added to the mixture while the mixing continued. The feedstocks were homogenised by passing them three times through a three-roll mill (EXAKT 3-roll mill 80E, EXAKT Advanced Technologies GmbH, Norderstedt, Germany) at 80 °C and 300 rpm. The feedstocks used for the characterisation and printing contained 40 vol% of solids loading. The optimal amounts of SA and S3, as determined by flow-curve measurements (see Section 2.3), were 1.25 and 2 mg/m^2, respectively. The surfactant ratios used to vary the extent of weak flocculation are presented in Table 1.

The interparticle net potentials were calculated for the case of zirconia particles of 340 nm when dispersed with SA or S3 using the Hamaker 2.2.2 program [22]. The Bergström model was used with a Hamaker constant of 3.39 $\times 10^{-20}$ J (in paraffin wax), a dielectric constant of 2.25, and a density of 0.9 g/cm^3 for the paraffin wax.

TG/DTA was performed using a Jupiter 449 simultaneous thermal analysis (STA) instrument (Netzsch, Selb, Germany) coupled with a 403 C Aëoloss mass spectrometer (Netzsch, Selb, Germany) for the analysis of the gases produced when heating the samples in Al_2O_3 (TG/DTA) crucibles with a heating rate of 10 °C/min in an argon/oxygen (80/20) atmosphere.

2.3. Rheological characterisation of feedstocks

A rheometer (Physica MCR 301, Anton Paar GmbH, Graz, Austria) was used to evaluate the rheological properties of the feedstocks. A cone-plate measuring system with a 25-mm diameter and an angle of 1.994° was used to avoid slipping.

The effect of the dispersant ratio of SA and S3 on the viscosity of the feedstock, to determine the optimal concentration used (Table 1), was measured on feedstocks with 35 vol% solid loading of zirconia and varying amounts of each dispersant (0.75−5 mg/m^2). The viscosity of the feedstocks was measured at 100 °C, with 60 points per interval, measured in 60 seconds with a shear-rate range of 0.01–1000 s^{-1}. The results obtained at a shear rate of 0.1 s^{-1} were plotted.

Prior to all the viscosity and yield stress measurements, the feedstocks were pre-sheared at 50 s^{-1} for 5 minutes at 100 °C, which was followed by a 5-minute rest step at 100 °C. The flow-curve behaviour of the feedstocks was determined by measuring the viscosity during the increase and immediate decrease (cycle) of the shear rate in the range 0.1−1000 s^{-1}. The temperature was held constant at 100 °C while 41 points per interval were measured. The measurements of each data point were made every 5 seconds at low shear rates and every 1 second at high shear rates. For each feedstock, three cycles were performed to check the repeatability.

For the yield stress measurements, the shear stress was increased from 0.01–1000 Pa while a data recording of shear strain was done with one data point per second. The presence of a sharp increase in the shear strain indicated the yield point of a certain feedstock.

The data obtained from the viscosity measurements were analysed using the Herschel–Bulkley [23,24] model. The model describes the dependence of the shear stress on the shear rate of the feedstock, according to the equation:

$$\tau = \tau_0 + K\dot{\gamma}^n \quad (1)$$

in which τ is the applied stress, $\dot{\gamma}$ is the shear rate, τ_0 is the yield stress, K is the consistency coefficient (also referred to as "Herschel–Bulkley viscosity"), and n is the flow behaviour index, with $n < 1$ for pseudoplasticity [25]. The fitting of the model curve (maximization of R^2 value) to the experimental data was performed with OriginPro® software using the Levenberg–Marquardt algorithm for nonlinear curve-fitting.

The storage and loss moduli of the feedstocks were evaluated. Feedstocks were pre-sheared at 50 s^{-1} for 5 minutes at 100 °C, which was followed by a 1-minute rest at 100 °C. Measurements were made at a

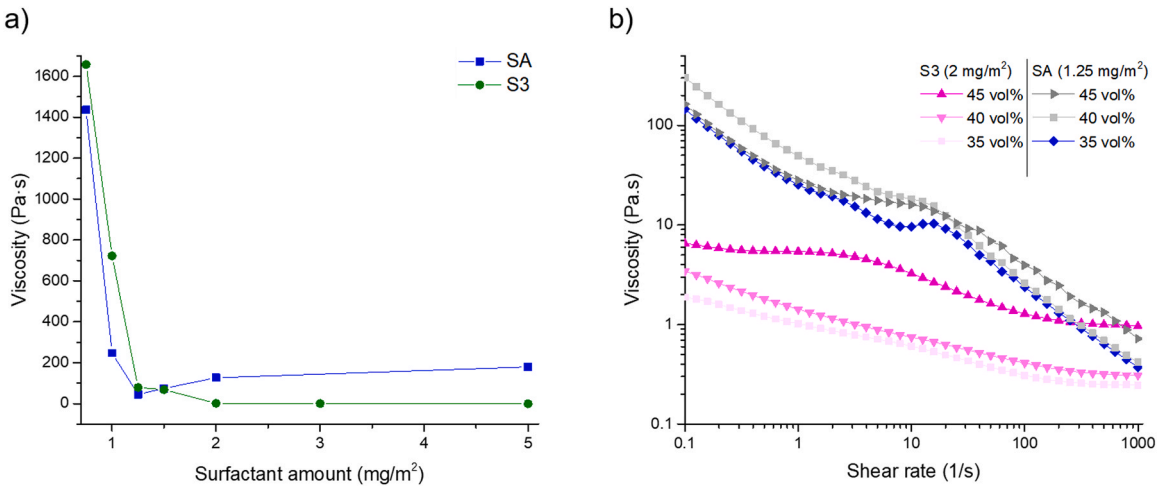

Fig. 1. a) Effect of surfactant amount on the viscosity of feedstocks containing 35 vol% zirconia, b) Effect of solids loading on the viscosity of the investigated feedstocks with optimal amount of surfactant (e.g., 1.25 mg/m^2 and 2 mg/m^2 for SA and S3, respectively).

constant shear strain of 1 % and a frequency of 1 Hz. A measuring step of 1 min per point was used from 100 °C to 65 °C with 5 °C intervals. Below 65 °C it was not possible to perform measurements as all the feedstocks were already solidified.

For the calculations of the Reynolds (*Re*) number, viscosity values at a shear rate of 10 s^{-1} and 100 °C were used. The jetting velocity was calculated using the needle radius (0.75 mm), nozzle diameter (200 μm), nozzle taper angle (90°), and needle speed (0.0144 m/s), following the equation previously defined in the literature for the calculation of droplet velocity [41]. Density values were taken as 2955 kg/m^3 for all the feedstocks, considering that the changes in the starting composition were minor and the densities of the used surfactants were comparable.

2.4. Feedstock extrusion by droplet jetting via T3DP

The feedstocks were deposited in the form of droplets using a microdispensing system (VERMES Microdispensing GmbH, Holzkirchen, Germany) attached to a 3D printer (HAGE3D 140 L, HAGE3D GmbH, Graz, Austria). A distance of 1.5 mm between the nozzle (with a diameter of 200 μm) and the print bed, as was previously recommended for drop-on-demand material-jetting systems, was employed [26]. A rising time (RT) of 7 ms, an open time (OT) of 0 ms, a falling time (FT) of 0.32 ms, a delay time (DT) of 10 ms, and a needle lift (NL) of 50 % were kept constant, which resulted in a deposition frequency of 57.7 Hz. The applied pressure at the cartridge was 1 bar. The nozzle and cartridge temperatures were set to 100 °C, while the travel speed of the nozzle head in the *x* and *y* directions was set to 100 mm/s, to allow for the observation of individual droplets.

Single-layer squares were printed for each feedstock, to observe the layer consistency and surface properties. For the printing of single layers, the same printing parameters as the printing of droplets were used. In this case, the travel speed was reduced, based on the droplet diameters, to ensure a droplet fusion of 50 % to ensure the deposition of lines and layers.

Printed green bodies with complex geometries were thermally wick-debinded in an alumina nanopowder (Sigma Aldrich) bed at 270 °C in a low-temperature furnace. Sintering was performed at 1450 °C for 2 hours in air in a high-temperature furnace.

2.5. Characterisation of printed droplets and single layers

The droplet-jetting process was recorded with a high-speed camera (Photron FASTCAM Mini UX100) using a frame rate of 20,000 fps, a shutter speed of 1/frame sec and resolution of 1280 ×248. The images were processed with Photron FASTCAM Viewer 4 software. A stereomicroscope (Discovery V8 - Carl Zeiss AG, Jena, Germany) and an optical microscope (Zeiss Axio Imager Z1m, Carl Zeiss AG, Jena, Germany) were used to observe the quality of the droplets and to measure their dimensions. The diameter of the droplets in the direction of printing ($d_{//}$) as well as in the direction perpendicular to the printing direction ($d_{\perp}$) were measured. The surface roughness of the printed single layers was measured using a profilometer (DektakXT stylus, Bruker, USA) with a 2-μm radius tip and a load of 1 mN. The resolution of 1 μm in the *y* direction was used to prepare images of 2 ×1 mm^2.

3. Results

3.1. Feedstock composition and thermal stability

The zirconia powder used in this study had a narrow particle size distribution (d_{50} = 0.34 μm) free of large agglomerates (Supplementary Figure S1a), also seen in Supplementary Figure S1b. The ceramic powders containing paraffin-wax slurries were in solid form at room temperature. Due to their thermoplastic behaviour, temperatures up to 100 °C were employed for their melting, characterization and deposition. According to the TG/DTA analysis, the melting temperature of the paraffin wax is ~65 °C (Supplementary Figure S2a), which is in accordance with the information provided by the manufacturer. The organic components were all stable up to ~200 °C, after which their decomposition begins. The melting behaviour of all the feedstocks was similar, regardless of the binder composition (Supplementary Figure S2b).

3.2. Rheological properties of feedstocks

To evaluate the effect of the surfactant concentration on the viscosity, feedstocks containing 35 vol% of ZrO_2 powder were prepared with various amount of surfactant added (Fig. 1a). In the case of SA, the lowest viscosity of 45 Pa·s at a shear rate of 0.1 s^{-1} was achieved when 1.25 mg/m^2 of SA was used. In the case of S3, a sharp decrease in the viscosity was observed when increasing the S3 concentration to 1.25 mg/m^2, similar to SA. In contrast to the latter, this was followed by a gradual viscosity decrease when increasing the S3 concentration to 2 mg/m^2 (recommended amount by the manufacturer), where the measured viscosity was 1.5 Pa·s. Afterwards, the viscosity was insensitive to any increase in S3, being around ~1 Pa·s.

The effect of solids loading on the viscosity of the feedstocks with a constant amount of surfactant was studied by gradually increasing the

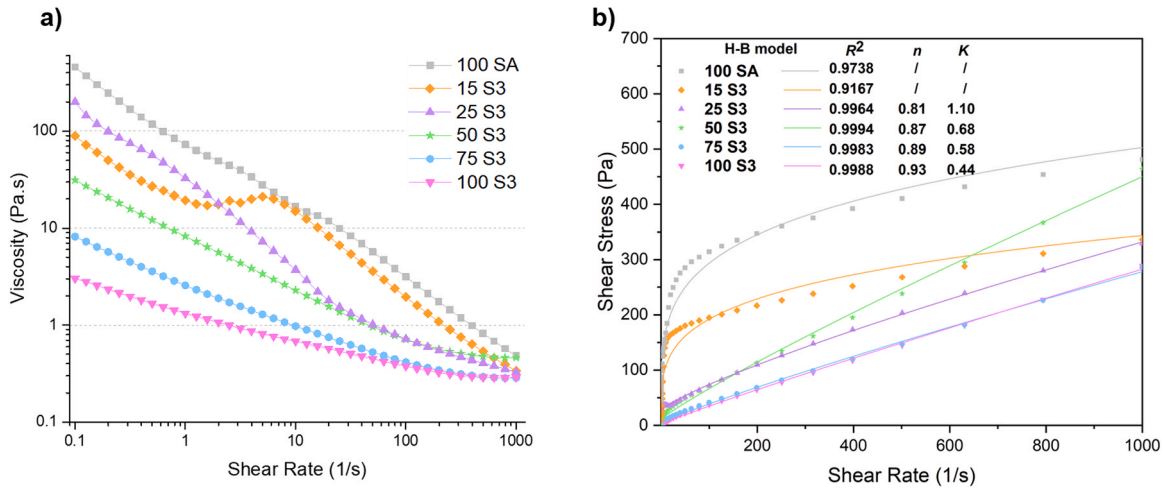

Fig. 2. a) Measurement of viscosity versus shear rate (flow-curve measurements) for feedstocks with various SA/S3 surfactant ratios, b) shear stress vs shear rate for feedstocks with various SA/S3 surfactant ratios, where the symbols represent experimental data and the solid lines are fits to the Herschel–Bulkley model.

solids loading from 35 vol% to 45 vol% (Fig. 1b). Feedstocks containing 50 vol% of solids could not be mixed successfully. As expected, an increase in the viscosity was observed when the solids loading was increased; however, different flow behaviour was observed for the suspensions stabilized with SA or S3. For the feedstocks dispersed with 1.25 mg/m^2 of SA, a discontinuous, non-monotonous flow behaviour was observed. At shear rates greater than 1 s^{-1} the flow deviated from the pseudoplastic, shear-thinning towards dilatant behaviour (Fig. 1b). The higher the concentration of SA, the more pronounced the non-monotonous discontinuity. The shear thickening behavior was followed by a second shear-thinning region at higher shear rates (>10−30 s^{-1}) that continued until the end of the measurement range was reached.

Feedstocks containing 2 mg/m^2 of S3 exhibited a less distinct shear-thinning behaviour with lower viscosity values at low shear rates. For feedstocks containing 45 vol% of solids loading a pseudo-Newtonian behaviour was observed at low shear rates, which gradually transitioned to shear thinning > 10 s^{-1}.

The rheological properties were measured for feedstocks with a combination of SA (2.4 nm) and S3 (10 nm) in different ratios (Table 1). Based on the results presented above a solids loading of 40 vol% was selected, as it was characterized by rheological properties in the acceptable range that was previously defined [11].

The flow of the majority of feedstocks exhibited a pseudoplastic shear thinning behaviour (Fig. 2a), where the overall viscosity decreased when the surfactant ratio favoured the S3. For feedstocks dispersed primarily with SA, i.e., 100 SA and 15 S3, a discontinuous, non-monotonous flow behaviour was observed, as described above for suspensions containing SA. For feedstocks with less than 75 % of SA, a continuous shear thinning throughout the measurement range was observed. At the highest shear rates, as the ratio of S3 was increased, a less distinct shear-thinning behaviour was observed and the behaviour of the feedstocks came closer to pseudo-Newtonian. Conversely, the 100 SA and 15 S3 did not exhibit such a transition and as a result, at a shear rate of 1000 s^{-1}, the viscosity decreased to values comparable with other feedstocks. Flow curves with all cycles of measurement are presented in Supplementary Figure S3.

The obtained flow curves of the feedstocks (40 vol%) for each surfactant variation were fitted with the Herschel–Bulkley (H-B) model (Fig. 2b), commonly used for suspensions with a high solids loading, which typically exhibit shear thinning and yield stress behaviour [27,28].

There is a distinct shift in the flow behaviour between feedstocks 100 SA and 15 S3, and the feedstocks containing a higher S3 content.

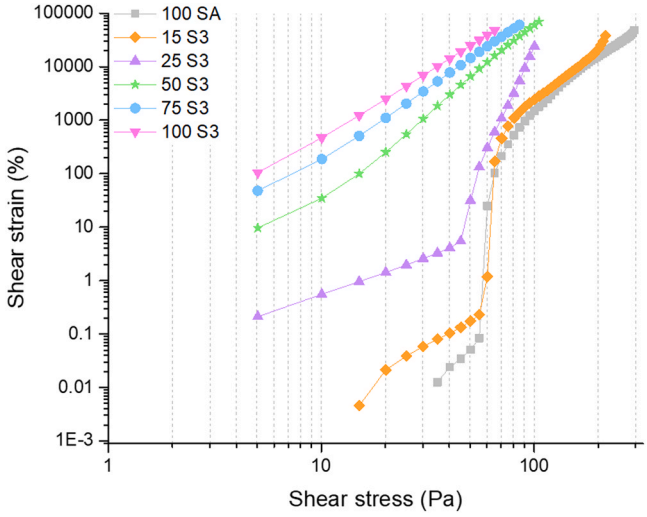

Fig. 3. Shear stress versus shear strain curves for the following feedstocks: 100 SA, 15 S3, 25 S3, 50 S3, 75 S3 and 100 S3.

Feedstocks 100 SA and 15 S3 exhibit a clear yield stress behaviour with a minimal increase in the shear rate with an initial increase in the shear stress up to a critical value of the shear stress when the suspensions begin to flow. On the other hand, suspensions containing a larger amount of S3 exhibit a nearly linear shear stress-shear rate response, with no apparent yield stress behaviour. The H-B model was successfully applied to determine the fitting parameters (τ_0, K, n) for the feedstocks with a higher S3 content (R^2 values >0.99) (Fig. 2b). Conversely, for feedstocks 100 SA and 15 S3, the maximum R^2 values were 0.97 and 0.92, respectively, indicating a poor fit of the experimental values to the H-B model. To evaluate the yield point of these feedstocks more accurately the intercept method was used (Fig. 3). All the feedstocks were characterized by a shear-thinning behaviour, as indicated by the flow index, n, which varied from a low n value ≈0.2 for the feedstock containing high SA surfactant, suggesting pronounced pseudoplastic behaviour, up to $n = 0.93$ indicating nearly Newtonian flow behaviour for the feedstock containing only S3 surfactant. A decrease in the consistency coefficient K, with increasing S3 content, is in accordance with the lower viscosities of these feedstocks (see Fig. 2a).

The effect of surfactant ratio on the yield stress was examined by measuring the shear strain with respect to the applied shear stress. High SA feedstocks (100 SA and 15 S3) had a yield point of 55 Pa. Increasing

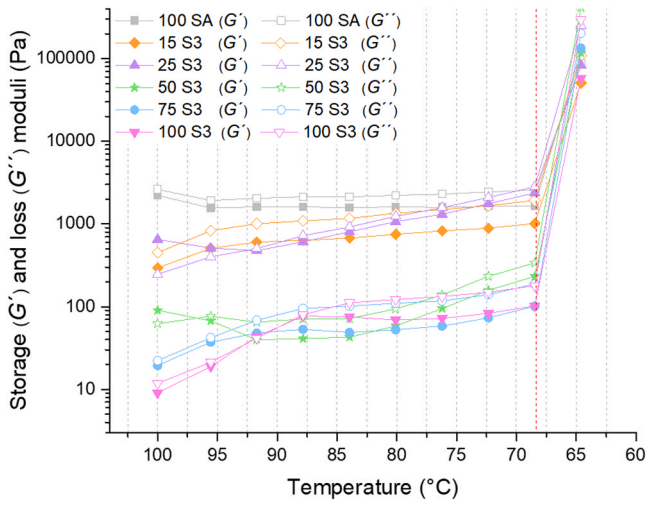

Fig. 4. Storage (G) and loss (G) moduli of feedstocks in relation to the temperature decrease.

the S3 amount to 25 % (25 S3) resulted in a yield stress value of 45 Pa. Feedstocks containing a larger amount of S3 did not exhibit yield stress behaviour, with continuous flow over the measuring range.

The viscoelastic properties of the feedstocks were analysed by measuring the storage (G) and loss (G) moduli during the temperature decrease from 100 °C to the point of solidification, i.e., lower than the melting temperature (Fig. 4). This was done to mimic the temperature (and rheological) change of the jetted droplets during their travel from the nozzle to the print bed. The 100 SA feedstock was practically insensitive to a temperature decrease in the range 100−70 °C, exhibiting a constant value for G´ and G´ of around 2000 Pa. The addition of 15–25 % of S3 to the feedstock composition decreased G´and G´, being in the 250−700 Pa range at an initial 100 °C. A further increase of S3 in the feedstocks resulted in a substantial decrease of G´ and G´ to the 10−100 Pa range. All the S3-containing feedstocks underwent a gradual increase of both moduli with a decrease of the temperature from 100 to 70 °C. Before solidification, low and high S3-containing feedstocks had G´ and G´ in the 80−250 and 1000−2500 Pa ranges, respectively, showing an order-of-magnitude difference depending on the composition of the dispersant. All the feedstocks had a sharp solidification transition at 67 °C (red dashed line in Fig. 4), which is in accordance with the melting temperature observed with TG/DTA (Supplementary Figure S2). Prior to solidification, G´ > G` was observed for all the feedstocks, which indicated a flow behaviour [29].

3.3. Droplet jetting and single-layer printing via T3DP

A high-speed camera was used to analyse the droplet formation during jetting with the T3DP (Fig. 5). Three distinct stages were observed: extrusion, spreading and droplet formation and/or

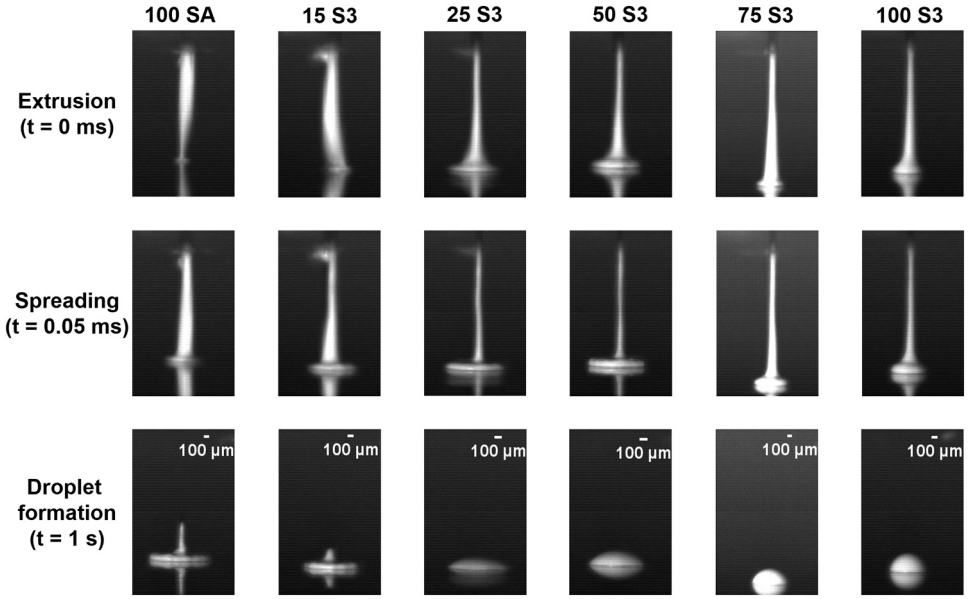

Fig. 5. Droplet formation during jetting with T3DP recorded by high-speed camera.

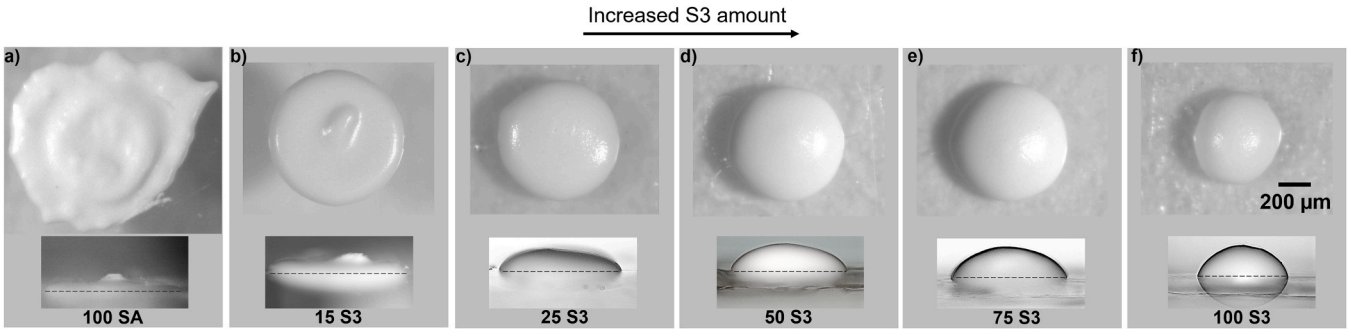

Fig. 6. Top and side optical micrographs of deposited droplets from suspensions: a)100 SA, b)15 S3, c) 25 S3, d) 50 S3, e) 75 S3 and f) 100 S3.

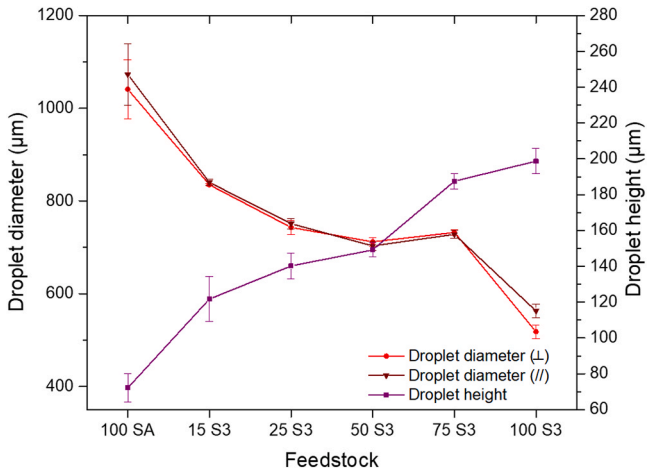

Fig. 7. Droplet diameter versus height with respect to feedstock composition.

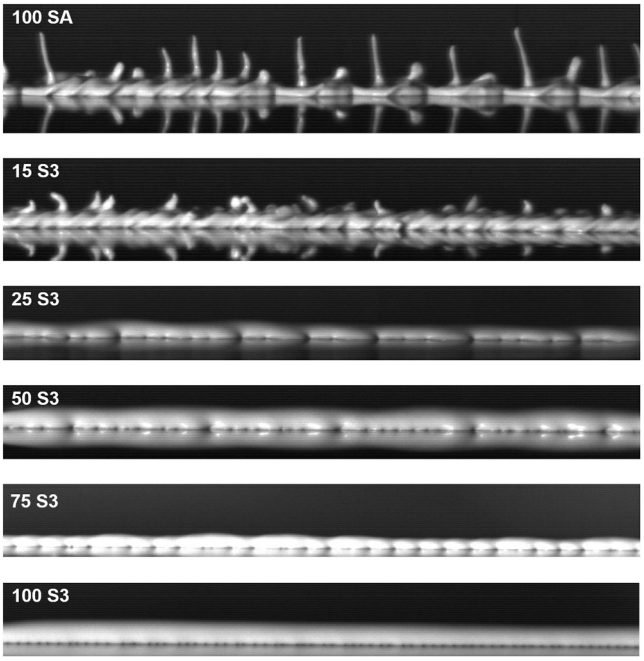

Fig. 8. High-speed camera images of deposited single lines formed from fused droplets jetted by T3DP from the following feedstocks: 100 SA, 15 S3, 25 S3, 50 S3, 75 S3 and 100 S3.

solidification. For all the feedstocks a continuous tail was formed following the extrusion of the droplet from the nozzle orifice, which receded only after the droplet was already deposited on the print bed. For the highest SA-containing feedstocks (100 SA, 15 S3), the tail geometry was inhomogeneous and asymmetrical. After deposition the droplets spread on the print bed, where the spreading was the lowest for feedstocks with the highest amount of S3. In the final stage, the tail collapsed and the droplet solidified in its final shape. In the case of 100 SA and 15 S3 the deposited material could not form a spherical droplet and was solidified with the remaining "tail" from the jetting event. For the remaining feedstocks the tail receded and a more spherical droplet was obtained.

A topographical analysis with a stereomicroscope (Fig. 6) further revealed that for feedstock 100 SA the droplets had a spatter morphology with a highly irregular edge (Fig. 6a). Furthermore, the deposition of feedstock 100 SA was disturbed after a short time due to the collection of the feedstock on the nozzle. The droplets deposited from feedstock 15 S3 had a more defined circular edge; however, flaws resulting from the collapsed droplet tail were observed in the centre (Fig. 6b). The diameter of the droplets in the printing direction ($d_{//}$) and perpendicular to the printing direction ($d_{\perp}$) decreased as the amount of surfactant with a longer chain (S3) was increased, while the opposite trend was observed for the droplet height. The diameter and height values obtained are shown in Fig. 7.

The fusing of the deposited droplets into lines and layers was evaluated by printing single lines (Fig. 8) and single-layer squares (Fig. 9). The defects on individual droplets are also clearly observed on the single lines formed from feedstocks 100 SA and 15 S3. Non-receded tails resulted in an inhomogeneous line with varying thickness and height. The quality of the lines formed with feedstocks containing more than 75 % S3 improved significantly. The lines formed from feedstocks 25 S3, 50 S3 and 75 S3 exhibited some minor differences in overlap and thickness, while lines formed from feedstock 100 S3 exhibited complete fusion between individual droplets to form a continuous line.

The printing of single layers was unsuccessful for feedstocks 100 SA (Fig. 9a) and 100 S3 (Fig. 9f) due to the high viscosity of the feedstock and the accumulation of the feedstock on the part, respectively. The printing of the remaining feedstocks resulted in a complete layer; however, this differed in terms of the quality of the printed parts. Namely, the printed layers from 15 S3 (Fig. 9b) and 25 S3 (Fig. 9c) were inhomogeneous, resulting in poor surface quality, especially at the end of the print (marked with yellow arrows in Figs. 9b and 9c). A high homogeneity in the surface texture and repeatability were achieved in single layers printed from the 50 S3 (Fig. 9d) and 75 S3 (Fig. 9e) feedstocks.

Profilometry was employed to quantitively assess the quality of the printed surface layers (excluding 100 S3). 3D surface-texture analyses with surface roughness are presented in Fig. 10. Indeed, the layers printed with the higher contents of SA (100 SA, 15 S3, 25 S3) showed high texture inhomogeneities and, consequently, the highest surface-area roughness values in the range 23−33 µm. In contrast, the 50 S3 and 75 S3 layers were more homogeneous, showing periodic lines of fused droplets. The smallest height deviation between the fused droplet lines (Sa value = 13.1 µm) was measured for the layer printed from feedstock 50 S3.

4. Discussion

4.1. The effect of surfactant composition on the (semi)steric stabilization of feedstocks

According to DLVO theory, the total potential energy (V_T) of a colloidal system is the sum of the van der Waals attraction (V_A) and the electrostatic repulsion (V_R) potentials between the colloidal particles dispersed in a solvent [30−33]. The use of surfactants introduces an additional parameter, i.e., steric repulsion (V_{ST}) (Eq. 2) [34,35].

$$V_T = V_{vdW} + V_{EL} + V_{ST} \quad (2)$$

In non-aqueous, wax-based ceramic feedstocks, there is limited V_{EL} potential, and the stearic barrier is needed. The chain length of the dispersant dictates V_T [16]. In the case of an insufficient chain length of the surfactant, a partial stabilization or "semi-steric" stabilization is achieved with V_{vdW} dominating [14,20]. It results in a network of weakly flocculated ceramic particles in the secondary minimum [19]. Consequently, there is a yield point, a critical stress inducing flow of the feedstock [36]. When shaping, the yield stress needs to be high enough for shape retention during debinding, but still allowing flow [15,16].

The SA and S3 used in the present study had 2.4 and 10 nm chain lengths, respectively. Feedstocks with varying amounts of both were also prepared to yield a steric barrier in between the lengths of the surfactants. The true length of the steric barrier affecting the V_{ST} will rely on the conformation of the adsorbed surfactant molecules, which

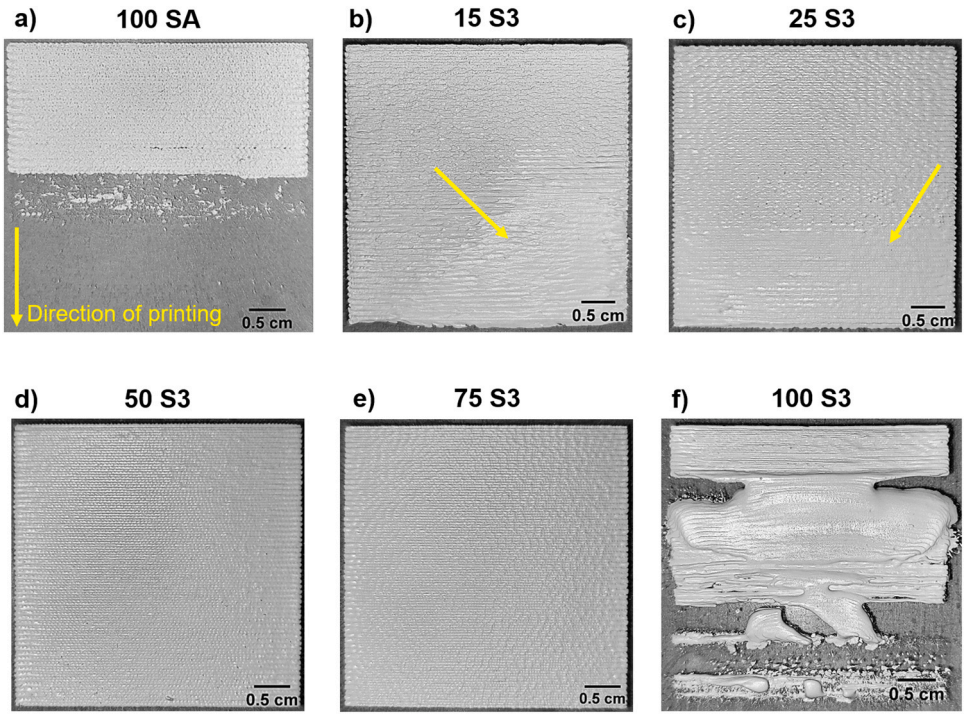

Fig. 9. Topographical view of single-layer squares printed from feedstocks: a)100 SA, b)15 S3, c) 25 S3, d) 50 S3, e) 75 S3 and f) 100 S3.

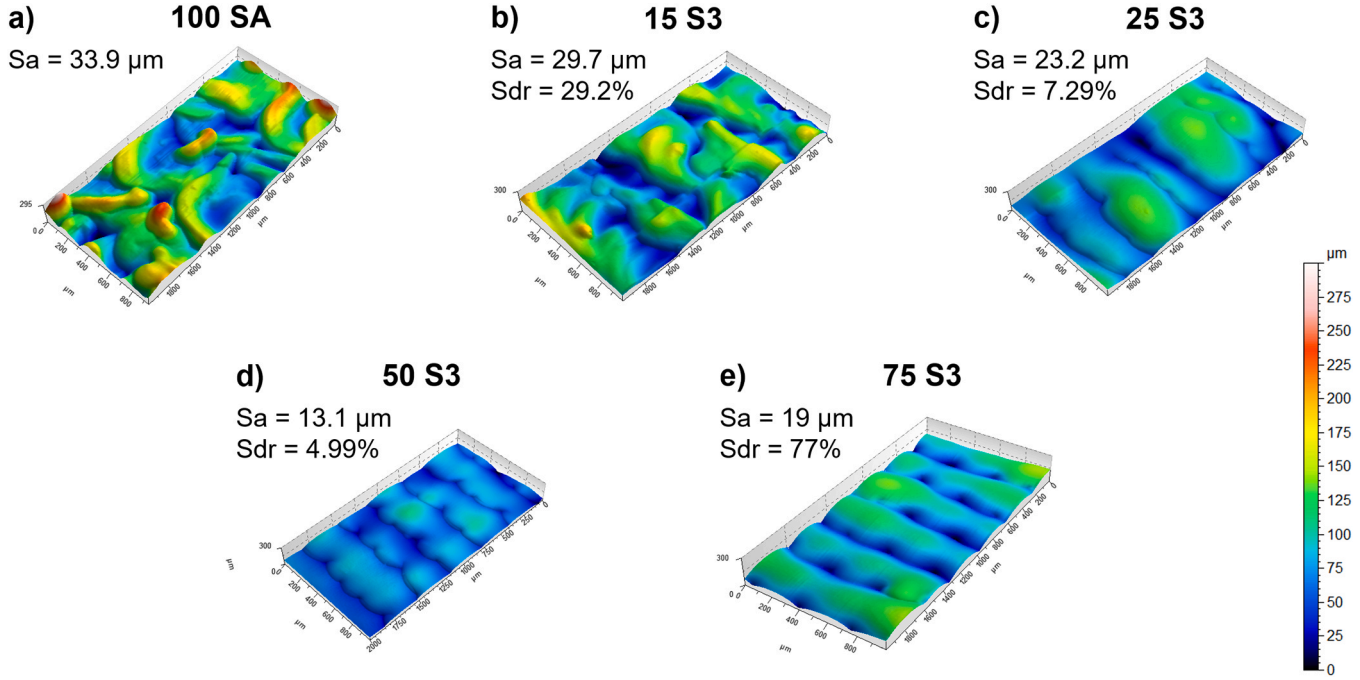

Fig. 10. Profilometry 3D surface textures with corresponding roughness values of single-layer squares printed from feedstocks: a)100 SA, b)15 S3, c) 25 S3, d) 50 S3 and e) 75 S3.

depend on factors such as solvent type, molecular structure, number of anchoring groups, the presence of other organics, etc. [37–39]. V_T was evaluated [22] for 340-nm zirconia particles dispersed in paraffin wax, if using SA or S3 as the dispersant, assuming a completely stretched configuration for simplicity (Fig. 11). In both dispersants, a secondary minimum is evident, indicating on a weak attraction (weak flocculation). However, the negative V_T potential obtained was six-times different, i.e., -19.7 vs -3.2 kT, as a result of the difference in the chain length. Consequently, the dispersion of feedstocks with different types of surfactant (and their mutual mixtures) will result in different rheological behaviour.

The relatively high attractive potential of the feedstocks stabilised predominantly with SA resulted in an increased apparent viscosity and yield stress. As a result, a continuous network of attractive particle agglomerates or weakly flocculated particle clusters throughout the suspension volume was formed [13]. A pronounced yield stress was observed for the feedstocks with the highest amount of SA (Fig. 3). This was the shear stress needed to achieve a yield point where the particles

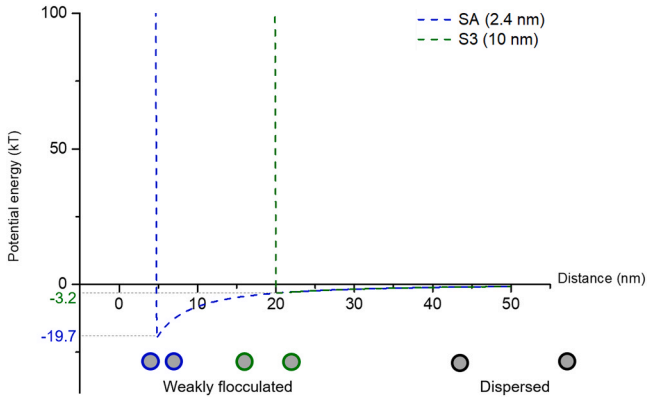

Fig. 11. Total potential energy between 340-nm zirconia particles adsorbed with SA or S3 in paraffin wax.

were sufficiently distanced and brought out from the secondary minimum to exert flow. The yield point value for S3-rich feedstocks (100−50 %) was not only lower, but the transition to flow was not sharp and was continuous. The shorter steric barrier layer in the SA-rich feedstocks was also responsible for the highest apparent viscosity levels achieved, especially in the low shear rate range 0.1−100 s^{-1}. The initial shear thinning that was observed for all the feedstocks was attributed to the breaking of the particle clusters and the formation of smaller flow units [32] as the shear rate increased. Moreover, the shorter steric barrier of the feedstocks containing 100 and 85 % SA was responsible for a discontinuous, non-monotonous flow, a short transition to dilatant, and shear thickening behaviour, occurring at 1−6 s^{-1} (Fig. 2a). The flow of concentrated colloidal suspensions, which under shear forms particulate layers sliding over each other, can be disrupted at a given shear rate. The disruption occurs due to the combination of the van del Waals forces and shear stress, thus the dilatant discontinuity arises [40,41]. Due to the flow discontinuity, poor fits of the shear stress-rate data were obtained using the Herschel–Bulkley model. A similar, non-monotonous behaviour was observed by Filip et al. [42] in polymer-based alumina feedstocks, stabilised with oleic acid, suitable for powder injection moulding. In this case an observed discontinuity in flow was observed at higher shear rates, higher viscosities and temperatures.

The magnitude of the continuous, weakly flocculated, attractive particle network influenced the storage (G) and loss (G) moduli, representing the elastic and viscous behaviour of the feedstocks, respectively [29]. It was interesting to observe that in the case of 100 SA both moduli were insensitive to temperature changes. With the increase of S3 in the surfactant ratio, larger interparticle distances and greater steric potentials [43] led to the expected decrease in G′/G″ moduli [18]. The increase in G′/G″ moduli with the temperature decrease for suspensions containing S3, was indicative of the decrease in interparticle distance in the particulate network and a higher attractive potential, possibly due to differences in the conformation and structuration of the polymeric steric barrier when S3 was present.

4.2. Droplet-formation dynamics during jetting of feedstocks

The T3DP process depends on the droplet-formation dynamics during the jetting of the feedstocks, which is governed by the rheological properties of the latter. During the jetting process of a non-Newtonian feedstock the droplet is formed through material extrusion, spreading and droplet formation through recoiling of the receded thin and long tail. Newtonian feedstocks are known to form satellite droplets as well as thick and short tails [44]. The dynamic viscosities of all the formulated feedstocks in this study were below the limiting viscosity values (<100−20 Pa·s at 10−100 s^{-1}, Fig. 2a) defined by Weingarten et al. [11] as a guideline for printable feedstock. However, the droplet-jetting process as well as the droplet geometries were greatly affected by the feedstock composition.

Table 2
Properties of zirconia feedstocks with 40 vol% of solids loading.

Feedstock	Viscosity Pa·s (@ 10 s^{-1})	*Re*	Yield stress* (Pa)	Yield stress** (Pa)	Printability of droplets
100 SA	16.7	0.014	55	/	Clogging, flaws
15 S3	14.9	0.016	55	/	Flaws
25 S3	3.7	0.064	45	27	Flaws
50 S3	2.2	0.1	/	6	Defect free
75 S3	0.9	0.265	/	3	Defect free
100 S3	0.6	0.398	/	2	Flaws

* Data obtained from yield stress measurement.
** Data obtained from Herschel-Bulkley model.

Jetting of the feedstocks containing the most SA (100−85SA) was marked by the inhomogeneous tail geometry, where the droplet could not form the deposited feedstock solidified with the remaining "tail" (Fig. 6a-b). T3DP exerts high shear rates (~4000–5000 s^{-1}) at the nozzle during jetting [11]. The pronounced shear thinning of these feedstocks, described by much lower n values (~0.25), reflects in substantially lower estimated stresses (and viscosities) at such high shear rates (see extrapolation in Fig. 2b), contributing to inhomogeneous spreading and extensive material flattening. Once on the printing bed with no external stress applied, the high yield stresses (55 Pa) were obviously higher than the surface energy within the short timeframe of cooling and solidification at 67 °C. Therefore, the droplet solidified before the receding of the tail and the formation of a droplet geometry. Droplet formation from suspensions with a high S3 content without the clear yield point value and with a monotonous shear-thinning behaviour (low K values and n = ~1) show strong dependency on the overall viscosity and G`/G″ moduli. The lower the viscosity and G`/G″ moduli, the smaller the diameter and larger the height of the formed droplets, respectively, where a lower droplet diameter was complemented by a larger droplet height, as all the jetted droplets had the same fixed volume.

The jetting of high-viscosity feedstocks where the inertial and viscous forces are dominant [45] can be represented by the Reynolds number (*Re*):

$$\mathrm{Re} = \frac{\upsilon \rho a}{\eta} \tag{3}$$

where ρ and η are the density and dynamic viscosity, υ is the velocity and a is the characteristic length, i.e., the diameter of the nozzle [46,47]. Table 2 presents data for the range where droplet jetting in the present study was possible. Based on the data and jetting experiment, printable droplets were achieved in the 0.1−0.265 *Re* range, which was lower than those defined in the literature for fluids printable by drop-on-demand systems [48].

4.3. Droplet fusion quality in the forming process of T3DP

The quality of the formed green body with T3DP relies on the adjustment of several dispensing parameters, such as those which affect the fusion factor (rising time, open time etc.), which will, given the thermoplastic properties of the feedstock, determine the shape, volume and homogeneity of the jetted droplet [49]. The dimensions of the droplets define the parameters for fusion into 1D lines and 2D layers in the layer-wise additive-manufacturing process [49]. In this respect, with the SA-rich feedstocks (100–85 % SA) it was not possible to print homogenous lines and layers (Figs. 8 and 9). Furthermore, clogging of the nozzle prevented the successful deposition of 2D layers for the 100 SA feedstock, which is known to occur if the viscosity at the nozzle is too high [11]. Any accumulation of material at the nozzle has to be avoided since it leads to the introduction of critical size defects in the formed

Fig. 12. Debinded and sintered parts after T3DP of 75 S3 feedstock.

ceramics [50,51]. Although the analysis of droplets and lines indicated good printability of the 100 S3 feedstock, the deposition of a single-layer square at given set printing parameters was not successful due to the formation of larger irregular areas of deposited material. A low feedstock viscosity and the absence of yield stress resulted in the accumulation of droplets into larger domains and a loss of resolution. However, adjusting printing parameters such as temperature (to lower feedstock`s viscosity), pressure and nozzle diameter, which were previously shown to affect the outcome of deposition [52], could result in homogenous printing of 2D layers from the 100 S3 feedstock, but was beyond the present study.

Feedstocks containing 25–75 % of S3 yielded the highest homogeneity and reliability during the deposition layers, with *Sa* values of 13−23 μm. Optimisation of the dispensing parameters could further improve the printing outcome, which was beyond the scope of this study. To demonstrate the complete ceramic manufacturing workflow, complex geometries were printed using feedstock 75 S3 (Fig. 12). The Archimedes relative densities were around 95 % (6.05 g/cm^3). The printed parts maintained their structural integrity during debinding although the feedstock used had no clear yield point value.

5. Conclusions

The present study evaluated how the chain length and surfactant composition affect the rheological properties of feedstocks used for T3DP applications. Decreasing the surfactant chain length from 10 nm to 2.4 nm resulted in a six-times-higher attractive potential energy (-3.2 kT vs -19.7 kT). The magnitude of the continuous, weakly flocculated, attractive particle network in feedstocks governed their viscosity, (non) monotonous shear thinning behaviour and yield stress as well as loss/storage modulus. These differences had a pronounced effect on the droplet-jetting dynamics, affecting droplet formation and shape, defining the final homogeneity and surface quality of the printed 2D layers. The guidelines for the processing of printable feedstocks for T3DP can be thus extended. It was possible to form homogeneous layers with the T3DP process when the feedstocks exhibited a monotonous shear thinning behaviour and when the yield stress, storage/loss modulus and *Re* number fall within range of below 45 Pa, 100−400 Pa and 0.1−0.265, respectively. This study broadens our understanding of the behaviour of non-Newtonian, thermoplastic ceramic feedstocks, which is crucial for successful droplet jetting used in T3DP technology.

CRediT authorship contribution statement

Andraž Kocjan: Writing – review & editing, Validation, Supervision, Funding acquisition, Formal analysis, Conceptualization. **Aljaž Iveković:** Writing – review & editing, Validation, Supervision, Formal analysis, Conceptualization. **Matevž Dular:** Methodology. **Milan Vukšić:** Writing – review & editing, Formal analysis. **Ipeknaz Özden Moser:** Writing – original draft, Methodology, Formal analysis, Conceptualization.

Declaration of Competing Interest

The authors declare that they have no known competing financial interests or personal relationships that could have appeared to influence the work reported in this paper.

Acknowledgement

This work was supported by the Slovenian Research Agency funding through the research project Preclinical and Clinical Investigations of Zirconia Dental Ceramics Fabricated by Additive Manufacturing Technologies (J3-3064), and the research programme Ceramics and Complementary Materials for Advanced Engineering and Biomedical Applications (P2-0087).

The authors thank Dr Marjeta Maček Kržmanc from the Jožef Stefan Institute, Advanced Materials Department, for her help with TG/DTA measurements and analysis. The authors also thank Dr Aljaž Drnovšek from the Jožef Stefan Institute, Department of Thin Films and Surfaces for his help with the profilometry analysis for the surface roughness.

Appendix A. Supporting information

Supplementary data associated with this article can be found in the online version at doi:10.1016/j.jeurceramsoc.2024.05.057.

References

[1] V. Lang, et al., Process data-based knowledge discovery in additive manufacturing of ceramic materials by multi-material jetting (CerAM MMJ), J. Manuf. Mater. Process. 4 (3) (2020), https://doi.org/10.3390/JMMP4030074.
[2] U. Scheithauer, et al., "Droplet-based additive manufacturing of hard metal components by thermoplastic 3D Printing (T3DP), J. Ceram. Sci. Technol. 8 (1) (2017) 155–160, https://doi.org/10.4416/JCST2016-00104.
[3] J.A. Lewis, J.E. Smay, J. Stuecker, J. Cesarano, Direct ink writing of three-dimensional ceramic structures, J. Am. Ceram. Soc. 89 (12) (2006) 3599–3609, https://doi.org/10.1111/j.1551-2916.2006.01382.x.
[4] D.H. Lee, B. Derby, Preparation of PZT suspensions for direct ink jet printing, J. Eur. Ceram. Soc. 24 (6) (2004) 1069–1072, https://doi.org/10.1016/S0955-2219(03)00421-7.
[5] I. Özden, U. Scheithauer, A. Iveković, A. Kocjan, Effect of infill strategy on the flexural strength of 3Y-TZP bars fabricated by thermoplastic 3D printing (T3DP), Open Ceram. 14 (2023), https://doi.org/10.1016/j.oceram.2023.100367.
[6] S. Novak, S.M.H. Olhero, J.M.F. Ferreira, A. Zupančič, Rheological properties of paraffin suspensions of surface-modified alumina powder for low-pressure injection moulding, Rheol. Acta 43 (5) (2004) 559–566, https://doi.org/10.1007/s00397-004-0401-8.
[7] S. Novak, A. Dakskobler, V. Ribitsch, The effect of water on the behaviour of alumina-paraffin suspensions for low-pressure injection moulding (LPIM), J. Eur. Ceram. Soc. (2000), https://doi.org/10.1016/S0955-2219(00)00083-2.
[8] K.A.M. Seerden, N. Reis, J.R.G. Evans, P.S. Grant, J.W. Halloran, B. Derby, Ink-jet printing of wax-based alumina suspensions, J. Am. Ceram. Soc. 84 (11) (2001) 2514–2520, https://doi.org/10.1111/j.1151-2916.2001.tb01045.x.
[9] X. Wang, W.W. Carr, D.G. Bucknall, J.F. Morris, High-shear-rate capillary viscometer for inkjet inks, Rev. Sci. Instrum. 81 (6) (2010), https://doi.org/10.1063/1.3449478.
[10] U. Scheithauer, E. Schwarzer, H.J. Richter, T. Moritz, Thermoplastic 3D printing - An additive manufacturing method for producing dense ceramics, Int. J. Appl. Ceram. Technol. (2015), https://doi.org/10.1111/ijac.12306.
[11] S. Weingarten, et al., Multi-material ceramic-based components - additive manufacturing of blackand- white zirconia components by thermoplastic 3D-printing (CerAM - T3DP), J. Vis. Exp. (2019), https://doi.org/10.3791/57538.
[12] S. Lu, X. Chen, H. Zheng, Y. Zhao, Y. Long, Simulation and experiment on droplet volume for the needle-type piezoelectric jetting dispenser, Micromachines 10 (9) (2019), https://doi.org/10.3390/mi10090623.
[13] L. Gorjan, Wick debinding - an effective way of solving problems in the debinding process of powder injection molding, Some Crit. Issues Inject. Molding (2012), https://doi.org/10.5772/34969.
[14] A. Dakskobler, T. Kosmač, Rheological properties of re-melted paraffin-wax suspensions used for LPIM, J. Eur. Ceram. Soc. (2009), https://doi.org/10.1016/j.jeurceramsoc.2008.11.012.
[15] F.A. Çetinel, W. Bauer, M. Müller, R. Knitter, J. Haußelt, Influence of dispersant, storage time and temperature on the rheological properties of zirconia-paraffin feedstocks for LPIM, J. Eur. Ceram. Soc. (2010), https://doi.org/10.1016/j.jeurceramsoc.2009.12.003.

[16] A. Dakskobler, A. Kocjan, P. Bowen, Predicting the yield stress of paraffin-wax suspensions, Powder Technol. 291 (2016) 1–6, https://doi.org/10.1016/j.powtec.2015.12.002.
[17] L. Gorjan, L. Reiff, A. Liersch, F. Clemens, Ethylene vinyl acetate as a binder for additive manufacturing of tricalcium phosphate bio-ceramics, Ceram. Int. 44 (13) (2018) 15817–15823, https://doi.org/10.1016/j.ceramint.2018.05.260.
[18] N.S. Bell, M.E. Schendel, M. Piech, Rheological properties of nanopowder alumina coated with adsorbed fatty acids, J. Colloid Interface Sci. 287 (1) (2005) 94–106, https://doi.org/10.1016/j.jcis.2005.01.113.
[19] R. Moreno, Better ceramics through colloid chemistry, J. Eur. Ceram. Soc. 40 (3) (2020) 559–587, https://doi.org/10.1016/j.jeurceramsoc.2019.10.014.
[20] D.M. Liu, Effect of dispersants on the rheological behavior of zirconia-wax suspensions, J. Am. Ceram. Soc. 82 (5) (1999) 1162–1168, https://doi.org/10.1111/j.1151-2916.1999.tb01890.x.
[21] D. Burnat, P. Ried, P. Holtappels, A. Heel, T. Graule, D. Kata, The rheology of stabilised lanthanum strontium cobaltite ferrite nanopowders in organic medium applicable as screen printed SOFC cathode layers, Fuel Cells 10 (1) (2010) 156–165, https://doi.org/10.1002/fuce.200900014.
[22] U. Aschauer, O. Burgos-Montes, R. Moreno, P. Bowen, Hamaker 2: a toolkit for the calculation of particle interactions and suspension stability and its application to mullite synthesis by colloidal methods, J. Dispers. Sci. Technol. 32 (4) (2011) 470–479, https://doi.org/10.1080/01932691003756738.
[23] T. Mezger, The Rheology Handbook: For Users of Rotational and Oscillatory Rheometers, Vincentz Network, Hannover, Germany, 2020.
[24] W.H. Herschel, R. Bulkley, Konsistenzmessungen von Gummi-Benzollösungen, Kolloid-Z. 39 (4) (1926) 291–300, https://doi.org/10.1007/BF01432034.
[25] M. Yarahmadi, P. Barcelona, G. Fargas, E. Xuriguera, J.J. Roa, Optimization of the ceramic ink used in Direct Ink Writing through rheological properties characterization of zirconia-based ceramic materials, Ceram. Int. 48 (4) (2022) 4775–4781, https://doi.org/10.1016/j.ceramint.2021.11.013.
[26] B. Derby, Additive manufacture of ceramics components by inkjet printing, Engineering 1 (1) (2015) 113–123, https://doi.org/10.15302/J-ENG-2015014.
[27] L. Gorjan, C. Galusca, M. Sami, T. Sebastian, F. Clemens, Effect of stearic acid on rheological properties and printability of ethylene vinyl acetate based feedstocks for fused filament fabrication of alumina, Addit. Manuf. 36 (2020) 101391, https://doi.org/10.1016/j.addma.2020.101391.
[28] B. Loebbecke, R. Knitter, J. Haußelt, Rheological properties of alumina feedstocks for the low-pressure injection moulding process, J. Eur. Ceram. Soc. (2009), https://doi.org/10.1016/j.jeurceramsoc.2008.11.001.
[29] L. del-Mazo-Barbara, M.P. Ginebra, Rheological characterisation of ceramic inks for 3D direct ink writing: a review, J. Eur. Ceram. Soc. 41 (16) (2021) 18–33, https://doi.org/10.1016/j.jeurceramsoc.2021.08.031.
[30] B. Derjaguin, L.D. Landau, Theory of the stability of strongly charged lyophobic sols and of the adhesion of strongly charged particles in solutions of electrolytes, Acta Physicochim. U. R. S. S. 14 (1941) 633–662.
[31] E.J.W. Verwey, J.T.G. Overbeek, Theory of the Stability of Lyophobic Colloids, Elsevier, *Amsterdam*, 1948.
[32] J.C. Chang, F.F. Lange, D.S. Pearson, Viscosity and yield stress of alumina slurries containing large concentrations of electrolyte, J. Am. Ceram. Soc. 77 (1) (1994) 19–26, https://doi.org/10.1111/j.1151-2916.1994.tb06952.x.
[33] S. Zürcher, T. Graule, Influence of dispersant structure on the rheological properties of highly-concentrated zirconia dispersions, J. Eur. Ceram. Soc. 25 (6) (2005) 863–873, https://doi.org/10.1016/j.jeurceramsoc.2004.05.002.
[34] E. Piacenza, A. Presentato, R.J. Turner, Stability of biogenic metal(loid) nanomaterials related to the colloidal stabilization theory of chemical nanostructures, Crit. Rev. Biotechnol. 38 (8) (2018) 1137–1156, https://doi.org/10.1080/07388551.2018.1440525.
[35] E.M. Hotze, T. Phenrat, G.V. Lowry, Nanoparticle aggregation: challenges to understanding transport and reactivity in the environment, J. Environ. Qual. 39 (6) (2010) 1909–1924, https://doi.org/10.2134/jeq2009.0462.
[36] S. Varchanis, et al., Transition between solid and liquid state of yield-stress fluids under purely extensional deformations, Proc. Natl. Acad. Sci. U. S. A. 117 (23) (2020) 12611–12617, https://doi.org/10.1073/pnas.1922242117.
[37] J.L. Ortega-Vinuesa, A. Martín-Rodríguez, R. Hidalgo-Álvarez, Colloidal stability of polymer colloids with different interfacial properties: mechanisms, J. Colloid Interface Sci. 184 (1) (1996) 259–267, https://doi.org/10.1006/jcis.1996.0619.
[38] R. Moreno, Colloidal processing of ceramic-ceramic and ceramic-metal composites, Process. Prop. Adv. Ceram. Compos. III 225 (2011) 147–159, https://doi.org/10.1002/9781118144442.ch13.
[39] D.H. Napper, Polymeric Stabilization of Colloidal Dispersions, Academic Press, 1983.
[40] R.L. Hoffman, Discontinuous and dilatant viscosity behavior in concentrated suspensions. II. Theory and experimental tests, J. Colloid Interface Sci. 46 (3) (1974) 491–506, https://doi.org/10.1016/0021-9797(74)90059-9.
[41] H.A. Barnes, A review of the slip (wall depletion) of polymer solutions, emulsions and particle suspensions in viscometers: its cause, character, and cure, J. Non Newton. Fluid Mech. 56 (3) (1995) 221–251, https://doi.org/10.1016/0377-0257(94)01282-M.
[42] P. Filip, B. Hausnerova, L. Cucova, On the Modelling of Non-monotonous Viscosity Describing Feedstock Behaviour in Powder Injection Moulding (2012) 192–195.
[43] A.R. Studart, E. Amstad, M. Antoni, L.J. Gauckler, Rheology of concentrated suspensions containing weakly attractive alumina nanoparticles, J. Am. Ceram. Soc. 89 (8) (2006) 2418–2425, https://doi.org/10.1111/j.1551-2916.2006.01087.x.
[44] Y. Son, C. Kim, Spreading of inkjet droplet of non-Newtonian fluid on solid surface with controlled contact angle at low Weber and Reynolds numbers,", J. Non Newton. Fluid Mech. 162 (1–3) (2009) 78–87, https://doi.org/10.1016/j.jnnfm.2009.05.009.
[45] X. Xiao, G. Li, T. Liu, M. Gu, Experimental study of the jetting behavior of high-viscosity nanosilver inks in inkjet-based 3D printing, Nanomaterials 12 (17) (2022), https://doi.org/10.3390/nano12173076.
[46] B. Derby, Inkjet printing ceramics: From drops to solid, J. Eur. Ceram. Soc. 31 (14) (2011) 2543–2550, https://doi.org/10.1016/j.jeurceramsoc.2011.01.016.
[47] H. Abdolmaleki, P. Kidmose, S. Agarwala, Droplet-based techniques for printing of functional inks for flexible physical sensors, Adv. Mater. 33 (20) (2021) 1–29, https://doi.org/10.1002/adma.202006792.
[48] B. Derby, Inkjet printing of functional and structural materials: fluid property requirements, feature stability, and resolution, 2010, doi: Annu. Rev. Mater. Res. 40 (2010) 395–414, https://doi.org/10.1146/annurev-matsci-070909-104502.
[49] U. Scheithauer, et al., Investigation of droplet deposition for suspensions usable for thermoplastic 3D printing (T3DP), J. Mater. Eng. Perform. (2018), https://doi.org/10.1007/s11665-017-2875-4.
[50] U. Scheithauer, A. Bergner, E. Schwarzer, H.J. Richter, T. Moritz, Studies on thermoplastic 3D printing of steel-zirconia composites, J. Mater. Res. 29 (17) (2014) 1931–1940, https://doi.org/10.1557/jmr.2014.209.
[51] J. Ebert, et al., Direct inkjet printing of dental prostheses made of zirconia, J. Dent. Res. 88 (7) (2009) 673–676, https://doi.org/10.1177/0022034509339988.
[52] S. Lu, G. Cao, H. Zheng, D. Li, M. Shi, J. Qi, Simulation and experiment on droplet formation and separation for needle-type micro-liquid jetting dispenser, Micromachines 9 (7) (2018), https://doi.org/10.3390/mi9070330.